Nonlinear hunting stability of high-speed railway vehicle on a curved track under steady aerodynamic load

Han Wu, Xiao-Hui Zeng, Jiang Lai & Yang Yu

Published online: 29 Jan 2019.

Submit your article to this journal

View Crossmark data

IA**VSD**

Taylor & Francis
Taylor & Francis Group

Check for updates

Nonlinear hunting stability of high-speed railway vehicle on a curved track under steady aerodynamic load

Han Wu[a,b], Xiao-Hui Zeng[a,b], Jiang Lai[c] and Yang Yu[d]

[a]Key Laboratory for Mechanics in Fluid Solid Coupling Systems, Chinese Academy of Sciences, Institute of Mechanics, Beijing, People's Republic of China; [b]School of Engineering Science, University of Chinese Academy of Sciences, Beijing, People's Republic of China; [c]Nuclear Power Institute of China, Chengdu, People's Republic of China; [d]State Key Laboratory of Hydraulic Engineering Simulation and Safety, School of Civil Engineering, Tianjin University, Tianjin, People's Republic of China

ABSTRACT

This paper investigates the nonlinear hunting stability of a high-speed vehicle on a curved track under steady aerodynamic load. We first established a nonlinear dynamic model of high-speed vehicle on a curved track while considering the effect of aerodynamic load. Then, we wrote a numerical simulation programme and verified the validity. The following two types of aerodynamic conditions were concerned in this study: considering only the aerodynamic lift and considering the crosswind loads. The influence of aerodynamic load on the creep force, the restoring force and moment generated by gravity, and the equilibrium position of the vehicle on the curved track can all change the hunting stability. We calculated bifurcation diagrams, limit cycle motions, nonlinear critical speeds, and frequency spectrum considering those two types of aerodynamic conditions, then compared with those without considering the aerodynamic effects. The results show that multiple frequencies including double frequency, triple frequency, quadruple frequency, and high frequencies will appear in addition to the fundamental frequency when hunting motion occurs. The higher frequencies which are even times of fundamental frequency are caused by the deviation of equilibrium position from track centre, while the deviation of equilibrium position is generated by curve track or crosswind load. Additionally, a positive aerodynamic lift and a crosswind load in the centrifugal direction will decrease the vehicle's motion stability, while a negative aerodynamic lift and a crosswind load in the centripetal direction can improve the stability.

1. Introduction

A railway vehicle moving along a track is a non-linear system that includes many coupled factors. It is very important to investigate the stability of the non-linear hunting motions of such a vehicle. There have been many important studies of the hunting stability of trains. True [1] provided an accurate definition of the non-linear critical speed and pointed out that this speed can be determined numerically by using the path-following method [2,3].

Polach and Kaiser [4] used two methods to analyse the non-linear hunting motion of a railway vehicle. Di Gialleonardo et al. [5] analysed the effects of different types of rail models on bifurcation diagrams. Zeng et al. [6] studied the gyroscopic effect of the wheelsets on the hunting stability of high-speed railway vehicles. Most of these studies focused on hunting stability on a straight track, but railway vehicles on a curved track experience very different operating conditions. Consequently, the non-linear stability of a vehicle on a curved track has also received attention. Using numerical simulations to produce bifurcation diagrams for such a system, Zboinski and Dusza [7,8] investigated the effects on the non-linear stability of the suspension parameters, the wheel/rail profile, wheel/rail wear, the radius of curvature of the track and the rail slope. Their studies [9] explained the cause of a train's self-excited vibrations and elucidated the similarity between a curved track and a straight track. Zeng and Wu [10] analysed the influence of the superelevation of the outer rail and of the radius of the curve on the non-linear critical speed. True et al. [11] calculated the critical speed of the curved track and studied the existence of multiple stable solutions of the curved-track problem. These studies have accordingly provided us with a theory of the non-linear stability of railway vehicles on curved tracks and also with appropriate numerical methods for calculating the non-linear critical speed.

Generally, the aerodynamic load is proportional to the square of the wind speed, and the aerodynamic load on a train generated by the reverse airflow and by crosswinds is considerably greater at higher speeds than at lower speeds. For this reason, it is crucial to investigate the aerodynamic loading effect on high-speed trains. Baker et al. [12,13], Yao et al. [14] and Sun et al. [15] conducted aerodynamic and flow-field analyses of high-speed trains. The analysis of the dynamic response and safety factors of high-speed train, aimed at aerodynamic loading conditions, has gradually taken root. Yu et al. [16] and Liu et al. [17] analysed the influence of aerodynamic loads on the dynamic response, derailment coefficient, the wheel load-reduction rate and the overturn coefficient. Cheng et al. [18,19] and Baker et al. [20] investigated the dynamic response and derailment coefficient of a railway vehicle under aerodynamic conditions. Mao [21] discussed the problem of vehicle control under crosswinds.

In summary, most numerical or experimental studies of the aerodynamic effects on high-speed railway-vehicle motions have been performed to obtain the aerodynamic load on the vehicle. The vehicle is then subjected to this load, and the dynamic response is analysed to obtain the derailment coefficient, load-reduction rate and derailment coefficient for the railway vehicle. These are actually forced-vibration problems. In contrast, the hunting stability of a railway vehicle subject to aerodynamic loads is a self-excitation vibration problem, the mechanism of which is different from that of forced vibrations. In other words, the results of existing studies of the aerodynamic loads on a vehicle's forced vibrations are not sufficient to characterise the stability of a vehicle's hunting motions under the influence of an aerodynamic load. It is therefore necessary to study the hunting stability of high-speed railway vehicles that are subject to aerodynamic loading effects. We have previously studied the linear stability of the aerodynamic effects on vehicles travelling on straight and curved tracks [22–25], and from these investigations we have gained considerable understanding of aerodynamic effects on the hunting stability of high-speed railway vehicles. A steady aerodynamic load can change the gravitational restoring force (and moment) and the creep force (and moment), as well as the equilibrium position of the moving vehicle. In the equations that describe vehicle motions, these effects appear as changes in the stiffness

and damping, which implies that the intrinsic characteristics of the vibration system of the high-speed rail vehicle have also changed.

In the present study, we have investigated the non-linear stability of a vehicle on a curved track, extending our previous linear-stability study. To understand the mechanism by which aerodynamic loading influences the hunting stability of a railway vehicle on a curved track, we consider here two aerodynamic conditions: steady aerodynamic lift and crosswind loads. Here, 'crosswind load' refers to the aerodynamic force and moment generated by a combination of high-speed reverse air flow and crosswinds on the train; this includes the lateral aerodynamic force, lift force, roll moment, pitch moment and yaw moment.

We first establish a non-linear dynamic model for a railway vehicle on a curved track that takes into account the aerodynamic load. We have developed a simulation programme based on this model, and we have verified the accuracy of this programme. Using this simulation programme, we have used a path-following method to calculate bifurcation diagrams for a railway vehicle that include the effects of aerodynamic lift and crosswind loads. By analysing the bifurcation characteristics, the non-linear critical speed and limit-cycle motions, we have determined the influence of aerodynamic effects on the non-linear hunting stability. In addition, we have analysed the frequency spectrum and determined the high-frequency characteristics of hunting motions on a curved track and under a crosswind load.

2. System model

2.1. Equations of motion

Figure 1 shows a dynamic model of a vehicle on a curved track, where C_0 is the superelevation of the outer rail, and the numbers represent the elements of the suspension system.

To investigate the hunting stability of a high-speed railway vehicle that is negotiating a curved track, we have considered 23 rigid-body degrees of freedom of the vehicle: the lateral displacement y_w and yaw ψ_w of the wheelset ($\times 4$), the lateral displacement y_t, vertical displacement z_t, roll ϕ_t, yaw ψ_t and pitch β_t of the frame ($\times 2$) and the lateral displacement y_c, vertical displacement z_c, roll ϕ_c, yaw ψ_c and pitch β_c of the car body ($\times 1$). These are collectively expressed in the vector Y_1:

$$Y_1 = [y_{w1} \quad y_{w2} \quad y_{w3} \quad y_{w4} \quad \psi_{w1} \quad \psi_{w2} \quad \psi_{w3} \quad \psi_{w4}$$
$$y_{t1} \quad z_{t1} \quad \phi_{t1} \quad \psi_{t1} \quad \beta_{t1} \quad y_{t2} \quad z_{t2} \quad \phi_{t2} \quad \psi_{t2} \quad \beta_{t2}$$
$$y_c \quad z_c \quad \phi_c \quad \psi_c \quad \beta_c]^{\mathrm{T}}. \tag{1}$$

The roll ϕ_w and vertical displacement z_w of the wheelset are not independent; they are constrained by the relative lateral displacement and the geometric relationship of the wheel and rail.

In addition, both the secondary lateral damping and the yaw damping are modelled by series-connected springs and dampers, and there are lateral displacements y_h of the spring-damped connecting points of the secondary lateral dampers ($\times 2$) and longitudinal displacements y_s of the spring-damper connecting points of the secondary yaw dampers
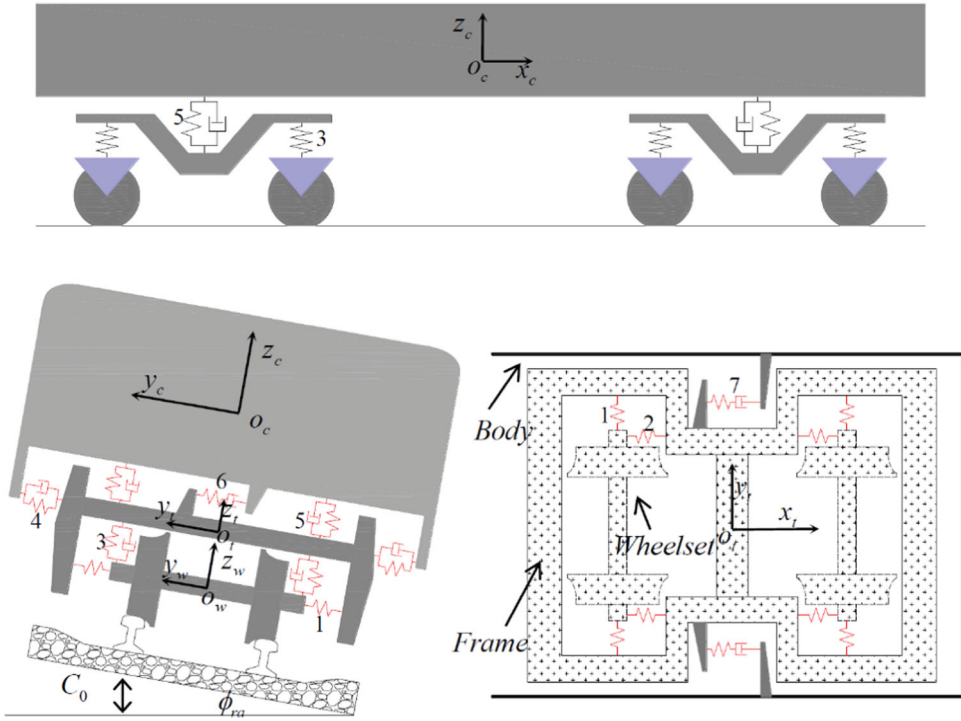
Figure 1. Schematic diagram of the dynamic railway-vehicle system. 1, 2 = primary lateral and longitudinal stiffness; 3 = primary vertical stiffness and damping; 4 = secondary lateral stiffness and damping; 5 = secondary vertical stiffness and damping; 6 = secondary lateral damping; and 7 = secondary yaw damping.

(×4). These degrees of freedom can be expressed collectively by the vector Y_2:

$$Y_2 = \begin{bmatrix} y_{h1} & y_{h2} & y_{sL1} & y_{sR1} & y_{sL2} & y_{sR2} \end{bmatrix}^T. \tag{2}$$

The equations of motions for this dynamical model can be written as follows:

$$M \begin{Bmatrix} \ddot{Y}_1 \\ 0 \end{Bmatrix} + C \begin{Bmatrix} \dot{Y}_1 \\ \dot{Y}_2 \end{Bmatrix} + K \begin{Bmatrix} Y_1 \\ Y_2 \end{Bmatrix} = P_f + P_g, \tag{3}$$

where M, C and K are the inertia matrix, damping matrix and stiffness matrix, respectively, and P_g and P_f denote the centrifugal and aerodynamic forces, respectively.

The individual governing differential equations are listed Appendix A, and all the physical quantities in Appendix A are defined in Appendix B. The nominal design parameters of the vehicle are also provided in Appendix B.

2.2. Wheel/rail contact relationship

2.2.1. Wheel/rail geometric profile

The non-linearity of the wheel-rail relationship is one of the most important non-linear factors of the railway-vehicle vibration system. In this paper, we use a combination of the tread profiles of the LMA wheel and the UIC60 rail.

2.2.2. Wheel and rail creep force

According to the Kalker theory of linear creep [26], the wheel/rail creep coefficients are as follows:

$$f_{11} = Gmn\left(\frac{3\pi(1-\sigma^2)}{2E(A+B)}N\right)^{\frac{2}{3}} C_{11}, f_{22} = Gmn\left(\frac{3\pi(1-\sigma^2)}{2E(A+B)}N\right)^{\frac{2}{3}} C_{22}$$

$$f_{23} = Gmn\left(\frac{3\pi(1-\sigma^2)}{2E(A+B)}N\right) C_{23}, f_{33} = Gmn\left(\frac{3\pi(1-\sigma^2)}{2E(A+B)}N\right)^{\frac{4}{3}} C_{33}$$

$$(A+B) = \frac{1}{2}\left(\frac{1}{R_w} + \frac{1}{r_r} + \frac{1}{r_w}\right) \tag{4}$$

where R_w, r_w, r_r, G, C_{ij}, m and n are the rolling radius of the wheelset, the transverse radius of the wheel profile, the transverse radius of the rail profile, the shear modulus, the non-dimensional Kalker coefficients and the coefficients about A and B, respectively. The coefficients C_{11}, C_{22}, C_{23} and C_{33} are tabulated elsewhere [27].

We calculate the creep force and creep moment according to Kalker's linear creep theory:

$$F_x = -f_{11}\gamma_x$$
$$F_y = -f_{22}\gamma_y - f_{23}\gamma_s$$
$$M_z = f_{23}\gamma_y - f_{33}\gamma_s, \tag{5}$$

where f_{11}, f_{22}, f_{23}, and f_{33} are creep coefficients, and γ_x, γ_y, and γ_s are creepages.

To calculate the wheel/rail creep force precisely, we used the Shen–Hedrick–Elkins non-linear creep model [28] and made the following corrections to the creep force:

$$F = \sqrt{F_x^2 + F_y^2}, \tag{6}$$

$$F' = \begin{cases} f \cdot N\left[\frac{F}{f \cdot N} - \frac{1}{3}\left(\frac{F}{f \cdot N}\right)^2 + \frac{1}{27}\left(\frac{F}{f \cdot N}\right)^3\right] & (F \le 3fN) \\ f \cdot N & (F > 3fN) \end{cases}, \tag{7}$$

where f is the coefficient of friction between the wheel and the rail. Introducing the correction factor ε defined by

$$\varepsilon = \frac{F'}{F}, \tag{8}$$

we can write the corrected creep force and creep moment as:

$$F'_x = \varepsilon \cdot F_x$$
$$F'_y = \varepsilon \cdot F_y$$
$$M'_z = \varepsilon \cdot M_z. \tag{9}$$

2.2.3. Wheel/rail normal force

The expression for the normal force at the wheel-rail contactcan be obtained from the equations for the rolling and vertical motions of the wheelset:

$$N_L = 2\cos(\lambda_L + \phi_w)(W + M_w\ddot{z}_w - F_{pzL} - F_{pzR} - f_{pzL} - f_{pzR}) +$$

$$\frac{2\cos(\lambda_L + \phi_w)}{d_0}\left(\begin{array}{l} I_{wx}\ddot{\phi}_w - I_{wy}\frac{v}{R_0}\left(\dot{\psi}_w - \frac{v}{R}\right) - d_{zx}F_{pzL} + d_{zx}F_{pzR} - d_{zx}f_{pzL} + d_{zx}f_{pzR} \\ -F_{yL}R_L - F_{yR}R_R - R_R N_R \sin(\lambda_R - \phi_w) + R_L N_L \sin(\lambda_L + \phi_w) \end{array}\right)$$

$$N_R = 2\cos(\lambda_R - \phi_w)(W + M_w\ddot{z}_w - F_{pzL} - F_{pzR} - f_{pzL} - f_{pzR}) -$$

$$\frac{2\cos(\lambda_R - \phi_w)}{d_0}\left(\begin{array}{l} I_{wx}\ddot{\phi}_w - I_{wy}\frac{v}{R_0}\left(\dot{\psi}_w - \frac{v}{R}\right) - d_{zx}F_{pzL} + d_{zx}F_{pzR} - d_{zx}f_{pzL} + d_{zx}f_{pzR} \\ -F_{yL}R_L - F_{yR}R_R - R_R N_R \sin(\lambda_R - \phi_w) + R_L N_L \sin(\lambda_L + \phi_w) \end{array}\right).$$

$$(10)$$

Here, N_L and N_R are, respectively, the normal forces at the left and right contact points; λ_L and λ_R are, respectively, the contact angles of the left and right wheels; R_L and R_R are, respectively, the radii of the rolling circles of the left and right wheels; and the quantities F_{pzL}, F_{pzR}, f_{pzL}, f_{pzR}, F_{yL} and F_{yR} are, respectively, the changes in the primary-suspension forces at the left and right sides of the wheelset, the primary-suspension damping forces at the left and right sides of the wheelset and the corresponding lateral creep forces.

In Equation (10), we calculate the roll ϕ_w and vertical displacement z_w of the wheelset from the geometric relationship between the wheel and rail and the lateral displacement of the wheelset. The normal force at the wheel/rail contact point is coupled to the various degrees of freedom of the motion; it is determined iteratively during the calculation.

2.3. Aerodynamic load

For a moving vehicle under the influence of a crosswind, the aerodynamic load on the vehicle is mainly caused by the high-speed airflow opposite to the forward direction of the vehicle and the ambient airflow. The aerodynamic loads are proportional to the square of the modulus of the sum of the two velocity vectors. The aerodynamic loads are given as:

$$F_{y\_wind} = \frac{1}{2}\rho A C_C(\vec{v}^2 + \vec{U}^2)$$

$$F_{z\_wind} = \frac{1}{2}\rho A C_L(\vec{v}^2 + \vec{U}^2)$$

$$M_{x\_wind} = \frac{1}{2}\rho A L C_{Mx}(\vec{v}^2 + \vec{U}^2)$$

$$M_{y\_wind} = \frac{1}{2}\rho A L C_{My}(\vec{v}^2 + \vec{U}^2)$$

$$M_{z\_wind} = \frac{1}{2}\rho A L C_{Mz}(\vec{v}^2 + \vec{U}^2) \qquad (11)$$

In Equations (11), ρ, A and L are the air density, reference area and reference length, respectively. The quantities C_C, C_L, C_{Mx}, C_{My} and C_{Mz} are the coefficients of the lateral aerodynamic force, lift force, roll moment, pitch moment and yaw moment, respectively.

The vectors $\vec{v}$ and $\vec{U}$ are the reverse air velocity (i.e. in the direction opposite to the vehicle velocity) and the crosswind velocity, respectively. The vector $\vec{U}$ can be in any direction, although, in practice, it is most commonly in the crosswind sense. If a train travels at a speed of 300 km/h, the reverse air speed is 83.3 m/s. Under normal operating conditions, the reverse air speed is much greater than the crosswind speed. Therefore, the reverse air flow plays a major role in determining the aerodynamic load.

The existence of a steady aerodynamic load has a major influence on the normal force on the wheel-rail system, because aerodynamic lift reduces the axle weight. The lateral aerodynamic force and the roll moment cause the normal forces on the left and right wheels to be different, and the pitch moment causes the normal force at the front wheel/rail contact point to be different from that at the rear wheel/rail contact point. The gravitational restoring force arises from the normal force between the wheel and the rail; a steady aerodynamic load thus changes the normal force and consequently changes the gravitational restoring force as well. In addition, the creep coefficient Equation (4) and correction factor Equation (8) are related to the normal force and the parameters of the contact point. Therefore, a steady aerodynamic load changes not only the normal force but also the equilibrium position of the wheel and rail. As a result, the creep coefficient and correction factor are changed significantly by the aerodynamic load and consequently so are the creep force and creep moment.

The changes in the gravitational restoring force and the creep force (and moment) due to a steady aerodynamic load appear in the equations of motion of the vehicle as changes in the stiffness and damping. This implies that the intrinsic characteristics of the vibration system of a high-speed railway vehicle also change. In other words, the effects of aerodynamic loads on a vehicle's vibration system are inherent and complex and are not just an external excitation.

2.4. Determining the non-linear critical speed

Because of the curved track and the aerodynamic load factors, the limit-cycle motion of a vehicle is asymmetric with respect to the centre of the track. In this paper, we construct the bifurcation diagram by plotting half of the peak-to-peak value of the lateral hunting motion as a function of vehicle speed.

Figure 2 is a subcritical bifurcation diagram for a typical non-linear railway-vehicle system. The minimum bifurcation speed v_n is the non-linear critical speed, and the larger bifurcation speed v_h is the Hopf bifurcation speed. A correct method for calculating the bifurcation diagram and finding the minimum bifurcation point is based on the path-following method [2]. In this method, we change the vehicle speed manually by a small step and solve the initial-value problem to obtain the dynamic response at each step. If the solution for the current step is stationary, then we increase the speed in the next step, and obtain the initial condition for the subsequent calculation by adding a small disturbance. The speed at which a periodic solution occurs is called the Hopf bifurcation speed v_h. The solution for the current step is then taken as the initial condition for the next step. We continue increasing the speed until the amplitude of the periodic solution is significantly large. We then decrease the vehicle speed by a small step. The smallest bifurcation point, i.e. the non-linear critical speed v_n, is found where the solution has a stable zero, as shown in Figure 2.
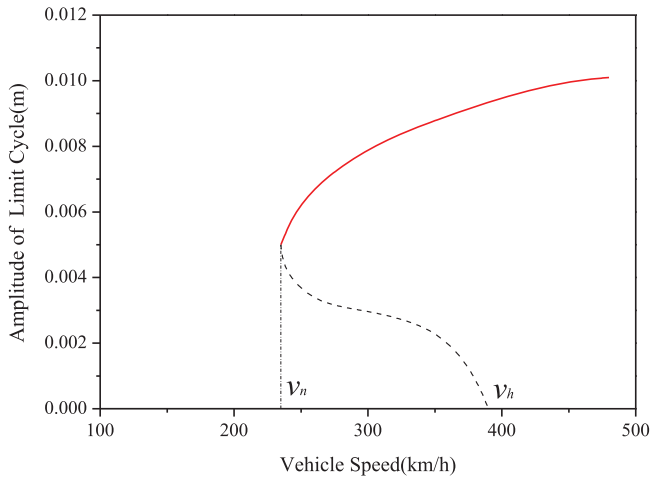
Figure 2. Schematic bifurcation diagram and the non-linear critical speed.

3. Simulation programme and validation

It is difficult to express the contact parameters as specific functions of the lateral displacement of the wheel relative to the rail. We therefore compute the wheel-rail profile at discrete data points and calculate the contact parameters using spline interpolation. We use the Runge-Kutta method to integrate the governing differential equations numerically to obtain the dynamic response, and we then calculate the bifurcation diagram, non-linear critical speed and motion phase diagram. To ensure the reliability of the simulation programme, we compared the simulation results with those obtained from commercial software and from the literature.

First, we examined the submodule for the wheel-rail contact relationship. Figure 3 compares the results calculated by this submodule with those obtained from commercial software for a LMA/UIC60 pair and from Ref. [29]. The results compare well, indicating that the submodule is correct.
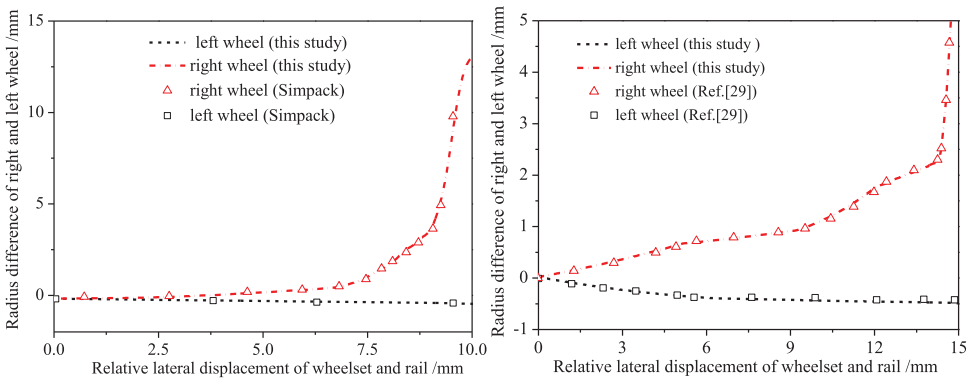

Figure 3. Comparison of the result from our non-linear wheel/rail subroutine with those from commercial software and from the literature.
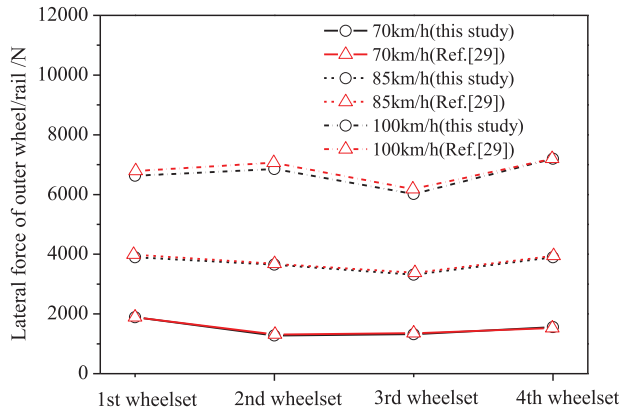
Figure 4. Comparison of wheel/rail lateral forces during steady-state motion on a circular track, as obtained from our simulation programme and from Ref. [29].
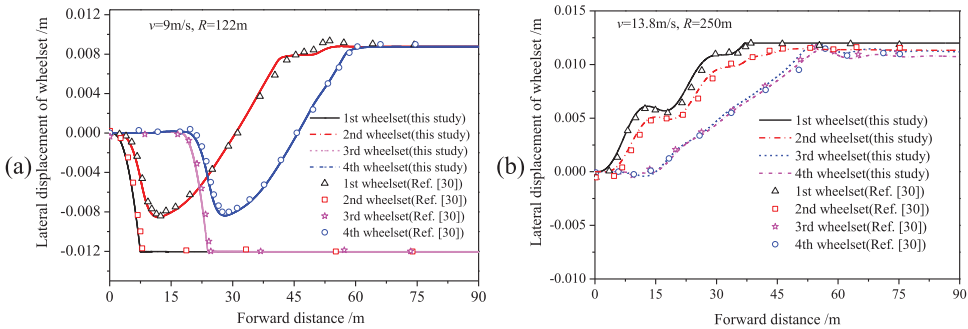

Figure 5. Comparison of the lateral displacements of wheelsets negotiating a curve, as obtained from our simulation programme and from Ref. [30]. (a) Ordinary railway vehicle. (b) Railway vehicle with simple turning mechanism.

In Figure 4, we compare the lateral wheel/rail forces on the outer track of a railway vehicle during steady-state motion on a circular track. The agreement is good for all three velocity conditions.

Fortin [30] calculated the lateral displacements of wheelsets during negotiation from a straight track onto a circular track for both an ordinary railway vehicle and a vehicle with a turning mechanism. We simulated the lateral displacement curves of the wheelsets using our simulation programme, and subsequently compared the results with Fortin's calculations, as shown in Figure 5. The results are consistent, thus again validating the accuracy of the programme developed in this study.

4. Non-linear bifurcation analysis

On the basis of our dynamic model and the simulation programme described above, we calculated the bifurcation diagram and the non-linear critical speed for a railway vehicle on a curved track. We assumed the radius of the true circular curve to be 6000 m and the

superelevation of the outer track to be 0.06 m. In the following discussion, we focus on two types of aerodynamic conditions: aerodynamic lift alone and crosswind loads.

4.1. Non-linear bifurcation analysis under aerodynamic lift

For aerodynamic lift, there are two cases: positive aerodynamic lift and negative aerodynamic lift. In our analysis, the positive aerodynamic lift coefficient is $C_L = 0.11563$, and the negative aerodynamic lift coefficient is $C_L = -0.12441$. When the effects of aerodynamic lift is not taken into account, $C_L = 0$.

Figure 6 shows bifurcation diagrams for the lateral movement of the first wheelset for a vehicle with positive aerodynamic lift, negative aerodynamic lift, and without any aerodynamic effect. In comparison to the case without any aerodynamic load, a positive aerodynamic lift increases the amplitude of the limit cycle and decreases the Hopf bifurcation speed and the non-linear critical speed. Conversely, a negative aerodynamic lift decreases the limit-cycle amplitude and increases the Hopf bifurcation speed and the non-linear critical speed. See Table 1 for details. Thus, a negative aerodynamic lift improves the stability of a railway vehicle on a curved track, whereas a positive aerodynamic lift degrades its stability.

Figure 7 shows the time history and phase-plane projections of the lateral displacement and yaw angle for the first wheelset at a speed of 290 km/h. The change in direction of the aerodynamic lift has a greater influence on the yaw than on the lateral displacement.
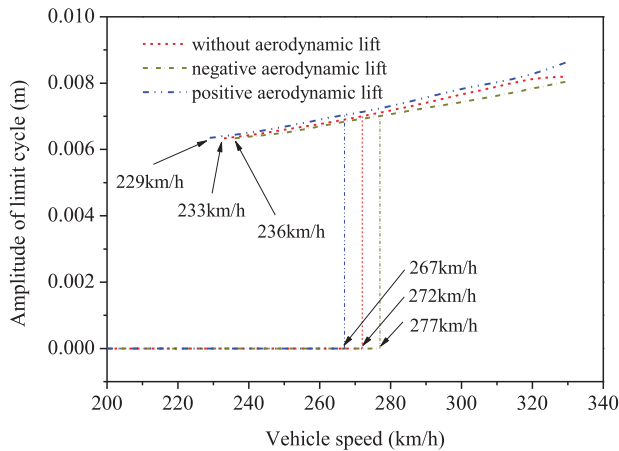

Figure 6. Comparison of bifurcation diagrams for the lateral displacement of the first wheelset.

Table 1. Changes in critical speed under the influence of aerodynamic lift.

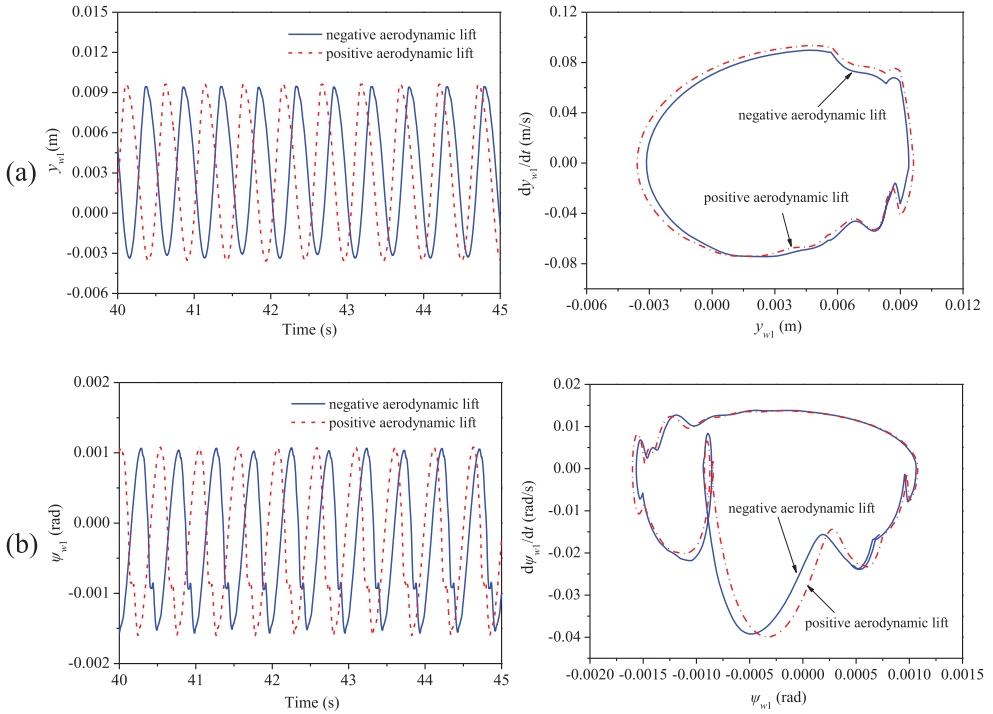|	Hopf bifurcation speed (km/h)	Non-linear critical speed (km/h)
Without aerodynamic load	272	233
Positive aerodynamic load ($C_L = 0.11563$)	267	229
Variation relative to $C_L = 0$	−5	−4
Negative aerodynamic load ($C_L = -0.12441$)	277	236
Variation relative to $C_L = 0$	+5	+3

Figure 7. Time history and phase-plane projection when $v = 290$ km/h. (a) First-wheelset lateral displacement. (b) First-wheelset yaw.

4.2. Non-linear bifurcation analysis under crosswind load

In this section, we consider further the complicated aerodynamic loads generated by crosswinds. On account of the curved track, we need to consider crosswinds in two opposite directions. One is a centrifugal crosswind, where the wind blows radially towards the outer rail of the track; the other is a centripetal crosswind, where the wind blows radially towards the inner rail of the track. To consider various wind directions and wind speed, we used the following five aerodynamic conditions in our calculations and analyses:

(1) Aerodynamic effects not considered: vf = 0.0 m /s.
(2) Centrifugal wind direction, wind speed at 10.7 m/s: vf = 10.7 m/s.
(3) Centrifugal wind direction, wind speed at 5.4 m/s: vf = 5.4 m/s.
(4) Centripetal wind direction, wind speed at 5.4 m/s: vf = −5.4 m/s.
(5) Centripetal wind direction, wind speed at 10.7 m/s: vf = −10.7 m/s.

We obtained the aerodynamic coefficients for the various aerodynamic conditions used in this section from Yang et al. [31]. These coefficients were calculated by the CFD method [15]. Table 2 shows all the aerodynamic coefficients. The difference between centrifugal and centripetal crosswinds is reflected in the opposite signs of C_C, C_{Mx} and C_{Mz}.

Table 2. Aerodynamic coefficients.

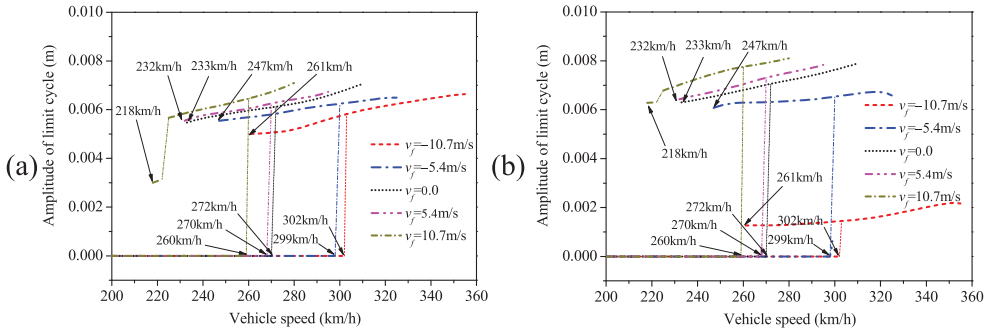| Aerodynamic condition	C_L	C_C	C_{Mx}	C_{My}	C_{Mz}
Centrifugal crosswind ($v_f = 10.7$ m/s)	−0.02797	0.33856	0.04379	−0.058333	−0.75349
Centrifugal crosswind ($v_f = 5.4$ m/s)	−0.10082	0.1358	0.01717	−0.24503	−0.74366
Centripetal crosswind ($v_f = -5.4$ m/s)	−0.10082	−0.1358	−0.01717	−0.24503	0.74366
Centripetal crosswind ($v_f = -10.7$ m/s)	−0.02797	−0.33856	−0.04379	−0.058333	0.75349

Figure 8. Bifurcation diagram for the lateral motion of (a) the first wheelset and (b) the third wheelset.

Table 3. Changes of critical speed under the influence of crosswind load.

	Hopf bifurcation speed (km/h)	Non-linear critical speed (km/h)
Without aerodynamic loads $v_f = 0$	272	233
$v_f = 10.7$ m/s	260	218
Variation relative to $v_f = 0$	−12	−15
$v_f = 5.4$ m/s	270	232
Variation relative to $v_f = 0$	−2	−1
$v_f = -5.4$ m/s	299	247
Variation relative to $v_f = 0$	+27	+14
$v_f = -10.7$ m/s	302	261
Variation relative to $v_f = 0$	+30	+28

We calculated the bifurcation diagram for a railway vehicle on a curved track for each of the five aerodynamic conditions listed above. Figure 8 shows the bifurcation diagrams for the lateral movement of the first wheelset and the third wheelset. These results show that the bifurcation diagram for a railway vehicle on a curved track has only one non-zero stable branch when considering the aerodynamic loads generated by crosswinds, which is the same as when the aerodynamic load effect is not considered. When the wind blows in the centripetal direction, the Hopf bifurcation speed and the non-linear critical speed increase. On the contrary, the Hopf bifurcation speed and the non-linear critical speed decrease under a centrifugal crosswind load. At a wind speed of 10.7 m/s, the changes in both the critical speed and the Hopf bifurcation speed are greater than those at a wind speed of 5.4 m/s. Table 3 shows the Hopf bifurcation speed and the non-linear critical speed for these five cases. The variations relative to the case without an aerodynamic load are shown in Table 3 as well. For a centrifugal crosswind at a speed of 10.7 m/s, the non-linear critical speed is 6.4% smaller than that without an aerodynamic load. Conversely, for
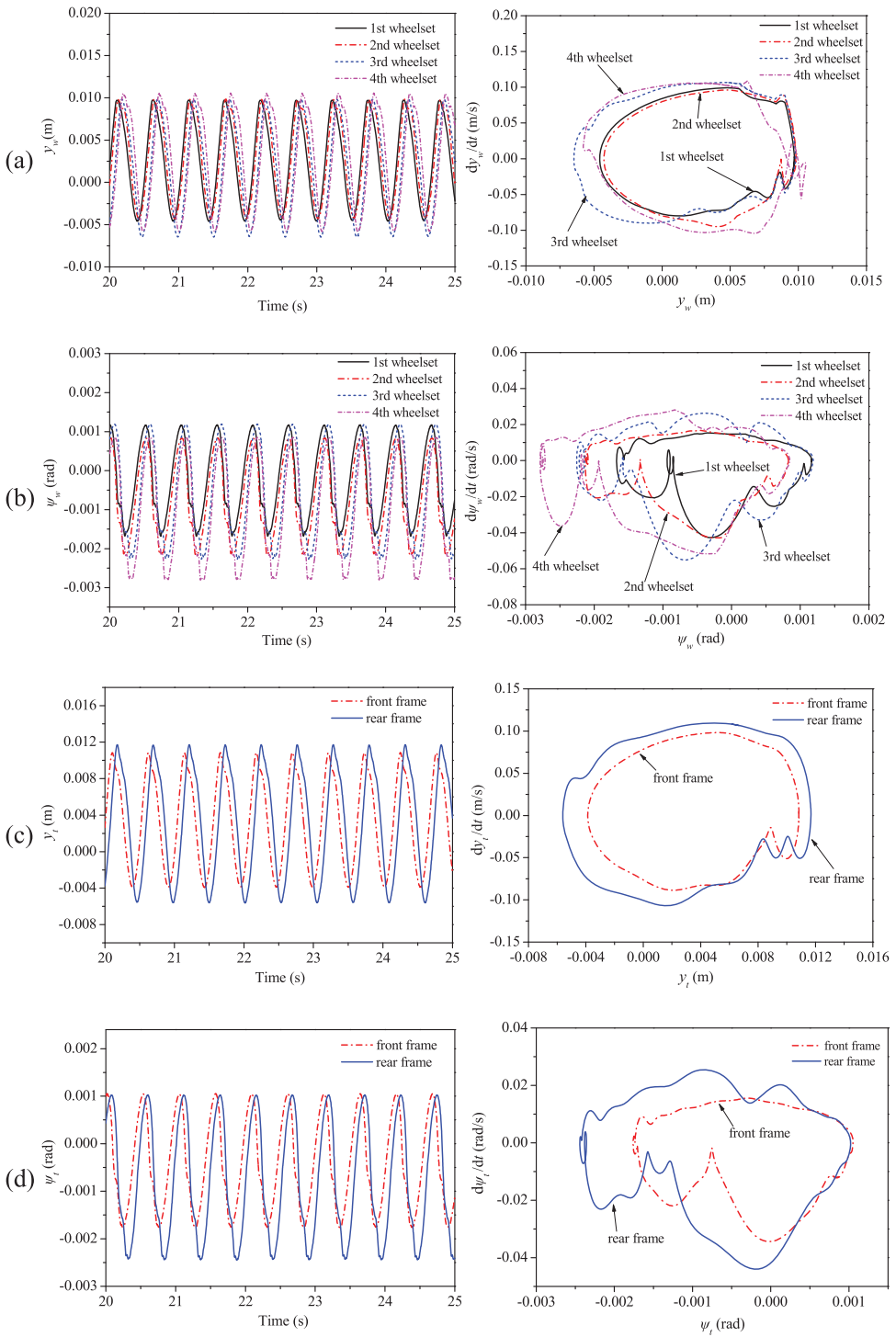
Figure 9. Time history and phase-plane projections for a vehicle moving at a speed $v = 280$ km/h and under a centrifugal crosswind $v_f = 10.7$ m/s. (a) Lateral displacement of the wheelsets. (b) Yaw of the wheelsets. (c) Lateral displacement of the frames, (d) Yaw of the frames.
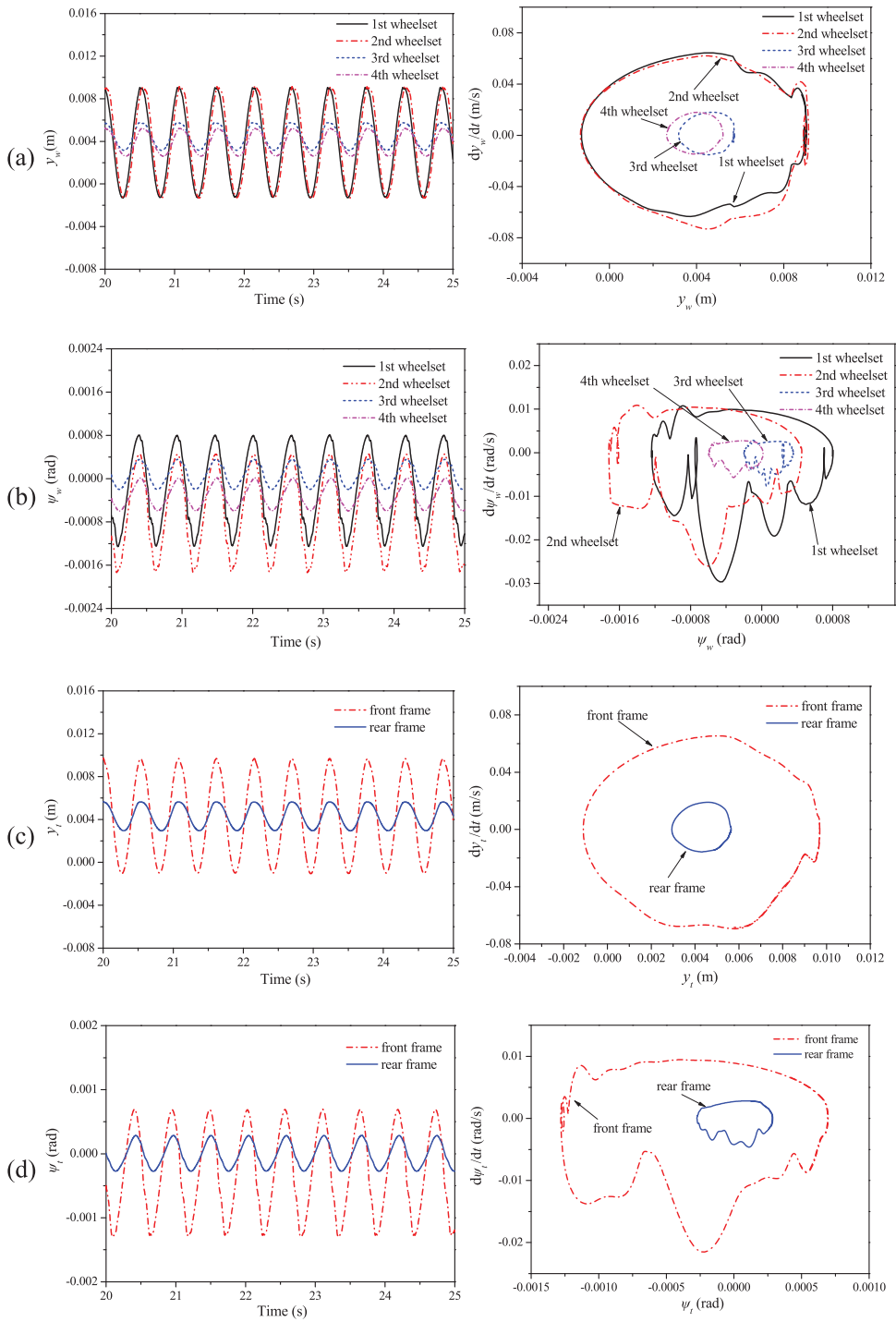
Figure 10. Time history and phase-plane projections of a vehicle moving at a speed $v = 280$ km/h and under a centripetal crosswind load with $v_f = -10.7$ m/s. (a) Lateral displacement of the wheelsets. (b) Yaw of the wheelsets. (c) Lateral displacement of the frames. (d) Yaw of the frames.

a centripetal crosswind at a speed of 10.7 m/s, the non-linear critical speed is 12% larger than that without an aerodynamic load.

Generally, for a fixed vehicle speed, a centrifugal crosswind load increases the amplitude of the limit cycle, whereas a centripetal crosswind decreases it. Figure 8 shows that a crosswind load of 10.7 m/s has a significant effect on the bifurcation diagram. If the wind direction is centrifugal, bifurcation exists in a small range of speeds (218–225 m/s) near the critical speed. Compared with a centrifugal wind load, the limit-cycle amplitude of the third wheelset decreases sharply when a centripetal wind load is considered

Figure 9 shows the time history and phase-plane projections of a vehicle moving at a speed of 280 km/h under a centrifugal crosswind load at $v_f = 10.7$ m/s. The results show that—when considering a crosswind blowing in the centrifugal direction—the amplitude of vibration of the front bogie (including the first and second wheelsets and the front frame) is smaller than that of the rear bogie (including the third and fourth wheelsets and the rear frame).

Figure 10 shows the time history and phase-plane projections of a vehicle moving at a speed of 280 km/h and under a centripetal crosswind load with $v_f = -10.7$ m/s. In a centripetal crosswind, the vibration amplitude of the front bogie is larger than that of the rear bogie. This is opposite to the case of a centrifugal crosswind load. This shows that a change in the wind direction can influence not only the non-linear critical speed but also the relative magnitude of the hunting motions of the front and rear bogies.

5. Frequency-spectrum analysis

To investigate the influence of aerodynamic loads on the vibration frequency of hunting motions, we used the fast fourier transform algorithm (FFT) to perform frequency-spectrum analyses of the wheelset motions. The sampling period was equal to the numerical integration step, 0.001 s. Thus, the sampling frequency was 1000 Hz, which meets the accuracy requirement of the FFT. Figure 11 shows the frequency spectrum of the first wheelset when limit-cycle motion occurs at a vehicle speed of 290 km/h, with aerodynamic
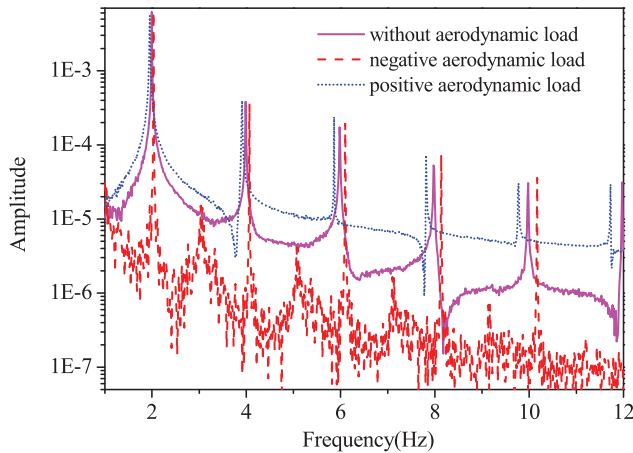

Figure 11. Spectrum of limit-cycle motions at a speed of 290 km/h, with aerodynamic lifts included.
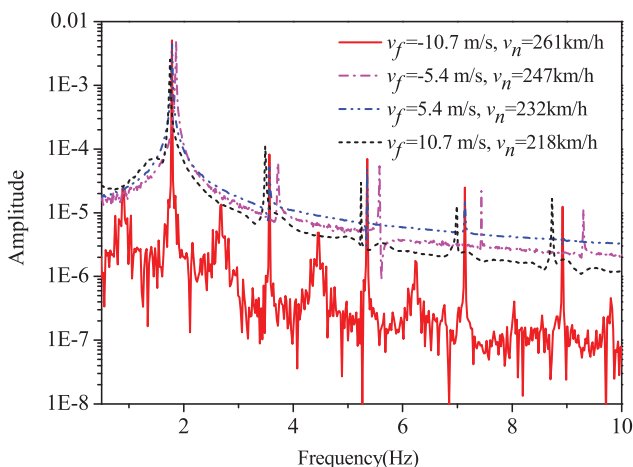
Figure 12. Spectrum at the non-linear critical speed under crosswind loads.

lifts included. The frequency spectrum at the non-linear critical speed under a crosswind load is shown in Figure 12. When hunting motion occurs, multiple frequencies appear in addition to the fundamental frequency, including the double frequency, triple frequency, quadruple frequency and higher frequencies.

Unlike a linear vehicle system, in a non-linear vehicle system, higher frequency vibrations occur at multiples of the fundamental frequency. In this section, we analyse the cause of the higher frequency vibrations for a vehicle subject to an aerodynamic load on a curved track. The non-linearity of our dynamic vehicle model is mainly rooted in the non-linear wheel/rail contacts. For simplicity, we analyse below the lateral movement of a wheelset. The relevant equation can be written in the simplified form

$$M_w \ddot{y}_w + F_k + F_f = N_R \cdot \lambda_R - N_L \cdot \lambda_L \tag{12}$$

where F_k and F_f are the primary-suspension force and the wheel/rail creep force, N_L and N_R are the left- and right-contact normal forces and λ_L and λ_R are the left and right contact angles, respectively.

We consider the LMA/UIC60 wheel/rail pair as an example. The relation between the wheel/rail contact angle and the lateral displacement y_w of the wheelset can be fitted with a polynomial function, as shown in Equations (13) and (14) and Figure 13. In Figure 13, $y_w = 0$ means that the wheelset is located at the centre of the track and that the wheel/rail contact point is located on the nominal rolling circle.

$$\begin{aligned}
\lambda_L = {} & 0.02496 + 0.1735(y_w - 0.02496) + 303.8388(y_w - 0.02496)^2 \\
& - 1.0555e6(y_w - 0.02496)^3 - 4.5476e8(y_w - 0.02496)^4 \\
& + 2.2664e12(y_w - 0.02496)^5 + 1.8239e14(y_w - 0.02496)^6 \\
& - 2.1008e18(y_w - 0.02496)^7 - 1.6998e19(y_w - 0.02496)^8 \\
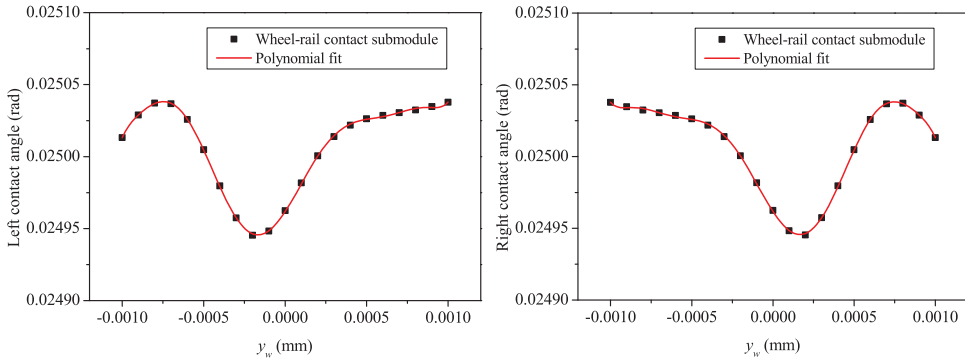& + 7.28745e23(y_w - 0.02496)^9
\end{aligned} \tag{13}$$

Figure 13. Polynomial fits for the left and right contact angles.

$$\lambda_R = 0.02496 - 0.1735(y_w - 0.02496) + 303.8388(y_w - 0.02496)^2$$
$$+ 1.0555e6(y_w - 0.02496)^3 - 4.5476e8(y_w - 0.02496)^4$$
$$- 2.2664e12(y_w - 0.02496)^5 + 1.8239e14(y_w - 0.02496)^6$$
$$+ 2.1008e18(y_w - 0.02496)^7 - 1.6998e19(y_w - 0.02496)^8$$
$$- 7.28745e23(y_w - 0.02496)^9 \tag{14}$$

When a vehicle is running on a straight, flat track without any aerodynamic load, its equilibrium position is located at the centre of the track, and the corresponding wheel/rail contact point is located on the nominal rolling circle. Then, the relationships between the contact angles and the relative lateral displacements of the left and right wheel/rail pairs are symmetrical, as shown in Figure 13. In the neighbourhood of the equilibrium position, the normal contact forces also can be regarded as equivalent; i.e. $N_L = N_R$. Substituting Equations (13) and (14) into Equation (12) and subtracting $N_R \cdot \lambda_R$ from $N_L \cdot \lambda_L$ causes the even terms in the polynomial to disappear, and only odd terms remain. However, if the vehicle is running on a curved track or under a crosswind load, its equilibrium position deviates from the centre of the track. Naturally, the normal contact forces in the neighbourhood of the equilibrium position then cannot be regarded as equivalent, and the relations between the contact angles and the relative lateral displacements of the wheel/rail pairs become unsymmetrical. In this case, both even and odd terms remain in the polynomial after $N_R \cdot \lambda_R$ is subtracted from $N_L \cdot \lambda_L$.

From this analysis, we conclude that only higher frequencies that are odd multiples of the fundamental frequency appear in the hunting motion when the equilibrium position is located at the centre of the track. Nevertheless, if the equilibrium position deviates from the track centre, then higher frequencies that are both even and odd multiples of the fundamental frequency appear in the hunting motion. The deviation from the equilibrium position may be caused either by the curved track or by the crosswind load. Although we obtained this conclusion by analysing the specific LMA/UIC60 pair, it can be extended to other wheel/rail pairs because the relationships between the contact angles and the relative lateral displacements of the left and right wheel/rail pairs are always symmetrical when the vehicle equilibrium position is located at the track centre.
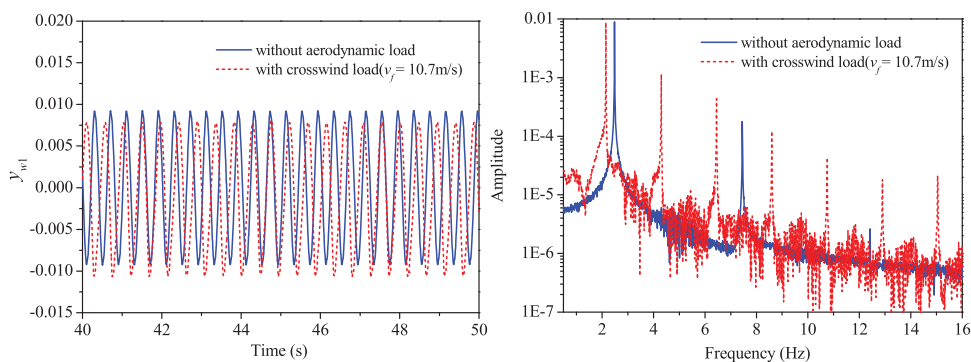
Figure 14. Time history and frequency spectrum for a vehicle at a speed of 550 km/h on a straight track.

To validate this conclusion, we simulated the hunting motion of a vehicle on straight track for cases both with and without aerodynamic loads, and we analysed the frequency spectrum. As shown in Figure 14, for a vehicle on a straight track and without an aerodynamic load, the equilibrium position is located at the centre of the track, and the high-frequency vibrations only contain frequencies that are odd multiples of the fundamental frequency. However, the equilibrium position deviates from the track centre when there is a crosswind load, and it is obvious that frequencies that are both even and odd multiples of the fundamental frequency exist in the hunting motion. These simulation results thus confirm our inference.

Our previous work [22–25] on the linear stability of a railway vehicle was performed using eigenvalue analysis, and we determined the influence of an aerodynamic load on the linear critical speed. In this paper, we give an explanation using explicit mathematical expression for the phenomenon that higher frequencies are multiples of fundamental frequency under actions of crosswind in nonlinear system.

6. Conclusion

A steady aerodynamic load changes the normal force at the various wheel-rail contact points, thus changing the creep force, gravitational restoring force and moment. This also changes the equilibrium position of the railway vehicle on the curved track. These aerodynamic effects change the stability of high-speed railway vehicles on a curved track. To investigate the effect of aerodynamic loads on the hunting stability of a vehicle on a curved track, we simulated the limit-cycle motions and bifurcation diagrams and obtained the critical speed for such a system. We also performed frequency-spectrum analyses and briefly discussed the mechanism responsible for the high-frequency characteristics of the hunting motion. From these analyses, we have drawn the following conclusions:

For a railway vehicle running on a curved track subject to aerodynamic loads, when hunting motions occur, multiple frequencies—including the double frequency, triple frequency, quadruple frequency and higher frequencies—as well as the fundamental frequency appear. In addition, a curved track or a crosswind load causes the equilibrium position to deviate from the track centre. In such cases, higher frequencies that are both even and odd multiples of the fundamental frequency appear in the hunting motion.

However, when the equilibrium position is located at the centre of the track, only higher frequencies that are odd multiples of the fundamental frequency appear.

A negative aerodynamic lift can improve the non-linear stability of a vehicle, whereas a positive aerodynamic lift can degrade the stability. Compared to a case without any aerodynamic load, a negative aerodynamic lift reduces the limit-cycle vibration amplitude of the various degrees of freedom of the railway vehicle. The greater the vehicle speed, the more pronounced the effect. Conversely, a positive aerodynamic lift increases the limit-cycle vibration amplitude.

A centrifugal crosswind load can lower the non-linear critical speed and the Hopf bifurcation speed of the vehicle. Conversely, a centripetal crosswind load can increase the non-linear critical speed and the Hopf speed. In one calculation, we assumed the radius of the curve to be 6000 m, the outer rail superelevation to be 0.06 m and the crosswind speed to be 10.7 m/s. For a centrifugal wind direction, the Hopf bifurcation speed is then reduced by 4.4%, and the non-linear critical speed is reduced by 6.4%. For a centripetal wind direction, on the contrary, the Hopf bifurcation speed is increased by 11.0%, and the non-linear critical speed is increased by 12.0%.

A change in the crosswind direction changes not only the non-linear critical speed but also the relative amplitude of the hunting motion of the front and rear bogies. At a wind speed of 10.7 m/s and a centrifugal wind direction, the hunting amplitude of the front bogie is smaller than that of the rear one. However, when the wind direction is centripetal, the hunting amplitude of the front bogie actually becomes greater than that of the rear bogie.

Disclosure statement

No potential conflict of interest was reported by the authors.

Funding

References

[1] True H. Does a critical speed for railroad vehicles exist? In: Railroad Conference. Proceedings of the 1994 ASME/IEEE Joint (in Conjunction with Area 1994 Annual Technical Conference); 1994 Mar 125–131.

[2] True H, Kaas-Petersen C. A bifurcation analysis of nonlinear oscillations in railway vehicles. Vehicle Syst Dyn. 1983;12(1–3):5–6.

[3] True H. Multiple attractors and critical parameters and how to find them numerically: the right, the wrong and the gambling way. Vehicle Syst Dyn. 2013;51(3):443–459.

[4] Polach O, Kaiser I. Comparison of methods analyzing bifurcation and hunting of complex rail vehicle models. J Comput Nonlin Dyn. 2012;7(4):041005.

[5] Di Gialleonardo E, Braghin F, Bruni S. The influence of track modelling options on the simulation of rail vehicle dynamics. J Sound Vib. 2012;331(19):4246–4258.

[6] Zeng XH, Wu H, Lai J, et al. The effect of wheel set gyroscopic action on the hunting stability of high-speed trains. Vehicle Syst Dyn. 2017;55(6):924–944.

[7] Zboinski K, Dusza M. Development of the method and analysis for non-linear lateral stability of railway vehicles in a curved track. Vehicle Syst Dyn. 2006;44(sup1):147–157.

[8] Zboinski K, Dusza M. Bifurcation approach to the influence of rolling radius modelling and rail inclination on the stability of railway vehicles in a curved track. Vehicle Syst Dyn. 2008;46(S1):1023–1037.

[9] Zboinski K, Dusza M. Self-exciting vibrations and Hopf's bifurcation in non-linear stability analysis of rail vehicles in a curved track. Eur J Mech A Solids. 2010;29(2):190–203.

[10] Zeng J, Wu PB. Stability analysis of high speed railway vehicles. JSME Int J Ser C. 2004;47(2):464–470.

[11] True H, Hansen TG, Lundell H. On the quasi-stationary curving dynamics of a railroad truck. Proceedings of the ASME/IEEE/AREA Joint Railroad Conference, ASME-RTD; 2005 Jan 131–138.

[12] Baker CJ. The simulation of unsteady aerodynamic cross wind forces on trains. J Wind Eng Ind Aerod. 2010;98(2):88–99.

[13] Baker C, Hemida H, Iwnicki S, et al. Integration of crosswind forces into train dynamic modelling. Proceedings of the Institution of Mechanical Engineers, Part F: Journal of Rail and Rapid Transit; 2011 Mar 154–164.

[14] Yao SB, Sun ZX, Guo DL, et al. Numerical study on wake characteristics of high-speed trains. Acta Mech Sin. 2013;29(6):811–822.

[15] Sun ZX, Yao SB, Guo DL, et al. Numerical study of crosswind stability of a high speed train. Sci Tech Engrg. 2012;12(32):8486–8497. in Chinese.

[16] Yu MG, Zhang JY, Zhang WH. Running attitudes of car body and wheelset for high-speed train under cross wind. Jiaotong Yunshu Gongcheng Xuebao. 2011;11(4):48–55. in Chinese.

[17] Liu JL, Yu MG, Zhang JY, et al. Study on running safety of high-speed train under crosswind by large eddy simulation. J China Railway Society. 2011;33(4):13–21. in Chinese.

[18] Cheng YC, Chen CH, Yang CJ. Dynamics analysis of high-speed railway vehicles excited by wind loads. Int J Struct Stab Dyn. 2011;11(06):1103–1118.

[19] Cheng YC, Huang CH, Kuo CM, et al. Derailment risk analysis of a tilting railway vehicle moving over irregular tracks under wind loads. Int J Struct Stab Dyn. 2013;13(08):1350038.

[20] Baker C, Cheli F, Orellano A, et al. Cross-wind effects on road and rail vehicles. Vehicle Syst Dyn. 2009;47(8):983–1022.

[21] Mao J, Xi YH, Yang GW. Research on influence of characteristics of cross wind field on aerodynamic performance of a high-speed train. J China Railway Society. 2011;33(4):22–30.

[22] Zeng XH, Lai J. Hunting stability of high-speed railway vehicle considering the actions of steady aerodynamic loads. Eng Mech. 2013;30(4):52–58. in Chinese.

[23] Zeng XH, Wu H, Lai J, et al. Influences of aerodynamic loads on hunting stability of high-speed railway vehicles and parameter studies. Acta Mech Sin. 2014;30(6):889–900.

[24] Zeng XH, Wu H, Lai J, et al. Hunting stability of high-speed railway vehicles on a curved track considering the effects of steady aerodynamic loads. J Vib Control. 2016;22(20):4159–4175.

[25] Zeng XH, Lai J, Wu H. Hunting stability of high-speed railway vehicles under steady aerodynamic loads. Int J Struct Stab Dyn. 2018;18(7):1850093.

[26] Kalker JJ. Three-dimensional elastic bodies in rolling contact. Dordrecht (ZH): Kluwer Academic Publishers; 1990.

[27] Kalker JJ. Survey of wheel-rail rolling contact theory. Vehicle Syst Dyn. 1979;8(4):317–358.

[28] Shen ZY, Hedrick JK, Elkins JA. A comparison of alternative creep force models for rail vehicle dynamic analysis. Vehicle Syst Dyn. 1983;12(1–3):79–83.

[29] Hirotsu T, Shimada M, Nishigaito T, et al. Curving simulation of a non-pendulum rail vehicle: 1st Report, The influence of Configurations and forced Steering. Trans of JSME Series C. 1999;65(637):3531–3538.

[30] Fortin C. Dynamic curving simulation of forced-steering rail vehicles [dissertation]. Kingston (ON): Queen's University; 1984.

[31] Yang GW, Jin XS, Wang YM, et al. Fundamental mechanics in high speed train at operation speed of 500 km/h, interim report. the National Basic Research Program of China (973 Program) 2012; library collection No.306-2014-010350. in Chinese (http://www.nstrs.cn/xiangxiBG.aspx?id = 50919).

Appendices

Appendix A. Equations of motion

(1) For the wheelsets,

$$
\begin{aligned}
m_w \ddot{y}_{wi} - 2k_{py}[-y_{wi} + y_{tn} + h_{tz}\phi_{tn} - (-1)^i l_t \psi_{tn}] = \\
- N_{Li}\sin(\lambda_{ri} + \phi_{wi}) + N_{Ri}\sin(\lambda_{li} - \phi_{wi}) + F_{yLi} + F_{yRi} \\
+ \frac{m_w v^2}{R_{wi}}\cos\phi_{rawi} - m_w g\phi_{rawi} + m_w R_0 \ddot{\phi}_{rawi} - m_w g\phi_{wi}
\end{aligned}
\tag{A1}
$$

$$
\begin{aligned}
I_{wz}\ddot{\psi}_{wi} + I_{wy}\frac{V}{R_0}(\dot{\phi}_w + \dot{\phi}_{ra}) + 2d_{zx}k_{px}[d_{zx}(\psi_{wi} + (-1)^i \Phi_{ai}) - d_{zx}\psi_{tn}] = \\
d_0\psi_{wi}[N_{Ri}\sin(\lambda_{ri} - \phi_{wi}) + N_{Li}\sin(\lambda_{li} + \phi_{wi})]\cos\psi_{wi} \\
+ d_0(F_{xRi} - F_{xLi}) + d_0\psi_{wi}(F_{yRi} - F_{yLi}) + M_{zRi} + M_{zLi} + I_{wz}v\frac{d}{dt}\left(\frac{1}{R_{wi}}\right)
\end{aligned}
\tag{A2}
$$

In Equations (A1) and (A2), $n = 1$ when $i = 1, 2$ and $n = 2$ when $i = 3, 4$. The subscript $i = 1 \sim 4$ represents the i-th wheelset, and $n = 1 \sim 2$ represents the n-th frame.

(2) For the frames,

$$
\begin{aligned}
m_t \ddot{y}_{ti} + 2k_{py}(2y_{ti} - y_{w(2i)} - y_{w(2i-1)} + 2h_{tz}\phi_{ti}) \\
- 2k_{ty1}(-y_{ti} + y_c + h_{tk}\phi_{ti} + h_{ck}\phi_c - (-1)^i l_c \psi_c) \\
- k_{ty2}(y_{hi} - y_{ti} + h_{th}\phi_{ti}) = \\
m_t\frac{v^2}{R_{ti}} - m_t g(\phi_{ti} + \phi_{ra}) + m_t(R_0 + h_t)\ddot{\phi}_{rati}
\end{aligned}
\tag{A3}
$$

$$
\begin{aligned}
m_t \ddot{z}_{ti} + 2k_{pz}(2z_{ti} - z_{w(2i)} - z_{w(2i-1)}) + 2c_{pz}(2\dot{z}_{ti} - \dot{z}_{w(2i)} - \dot{z}_{w(2i-1)}) \\
- 2k_{tz1}[z_c - z_{ti} + (-1)^i l_c \beta_c] = -m_t d_0 \ddot{\phi}_{ra}
\end{aligned}
\tag{A4}
$$

$$
\begin{aligned}
I_{tx}(\ddot{\phi}_{ti} + \ddot{\phi}_{rati}) + 2k_{py}h_{tz}(y_{w(2i-1)} + y_{w(2i)} - 2y_{ti} - 2h_{tz}\phi_{ti}) \\
+ 2k_{pz}d_{zx}^2(2\phi_{ti} - \phi_{w(2i-1)} - \phi_{w2i}) - 2c_{pz}d_{zx}^2(2\dot{\phi}_{ti} - \dot{\phi}_{w(2i-1)} - \dot{\phi}_{w2i}) \\
- 2h_{tk}k_{ty1}[y_{ti} - y_c - h_{tk}\phi_{ti} - h_{ck}\phi_c + (-1)^i l_c \psi_c] \\
+ h_{th}k_{ty2}(y_{hi} - y_{ti} + h_{th}\phi_{ti}) + 2d_{kh}^2 k_{tz1}(\phi_{ti} - \phi_c) = 0
\end{aligned}
\tag{A5}
$$

$$
\begin{aligned}
I_{tz}\ddot{\psi}_{ti} - 2k_{py}l_t(y_{w(2i-1)} - y_{w(2i)} - 2l_t\psi_{ti}) - 2k_{px}d_{zx}^2(\psi_{w(2i-1)} + \psi_{w(2i)} - 2\psi_{ti}) \\
- d_{sx}k_{sx}[y_{sRi} - y_{sLi} - 2d_{sx}(\psi_{ti} + (-1)^i \Phi_{si})] \\
- 2d_{kh}^2 k_{tx1}[\psi_c - \psi_{ti} - (-1)^i \Phi_{si}] = I_{tz}v\frac{d}{dt}\left(\frac{1}{R_{ti}}\right)
\end{aligned}
\tag{A6}
$$

$$
\begin{aligned}
I_{ty}\ddot{\beta}_{ti} - 2l_t k_{pz}(-z_{w(2i-1)} + z_{w(2i)} - 2l_t\beta_{ti}) - 2l_t c_{pz}(-\dot{z}_{w(2i-1)} + \dot{z}_{w(2i)} - 2l_t\dot{\beta}_{ti}) \\
+ 4h_{tz}^2 k_{px1}\beta_{ti} + h_{ts}k_{sx}(2h_{ts}\beta_{ti} + y_{sLi} + y_{sRi}) + 2h_{tk}k_{tx1}(h_{ck}\beta_c + h_{tk}\beta_{ti}) = 0
\end{aligned}
\tag{A7}
$$

In Equations (A3) $\sim$ (A7), $i = 1 \sim 2$ represents the i-th frame.

(3) For the carbody,

$$m_c \ddot{y}_c - 2k_{ty1}(y_{t1} + y_{t2} - 2y_c - h_{tk}\phi_{t1} - h_{tk}\phi_{t2} - 2h_{ck}\phi_c)$$
$$+ k_{ty2}(-y_{t1} + h_{th}\phi_{t1} + y_{h1}) + k_{ty2}(-y_{t2} + h_{th}\phi_{t2} + y_{h2}) =$$
$$m_c \frac{v^2}{R_c} - m_c g(\phi_c + \phi_{rac}) + m_c h_c \ddot{\phi}_{rac} + F_{y\_wind} \tag{A8}$$

$$m_c \ddot{z}_c + 2k_{tz1}(2z_c - z_{t1} - z_{t2}) = -m_c d_0 \ddot{\phi}_{rac} + F_{z\_wind} \tag{A9}$$

$$I_{cx}(\ddot{\phi}_c + \ddot{\phi}_{rac}) - 2k_{ty1}h_{ck}(y_{t1} + y_{t2} - 2y_c - h_{tk}\phi_{t1} - h_{tk}\phi_{t2} - 2h_{ck}\phi_c)$$
$$+ h_{ch}k_{ty2}(-y_{t1} + h_{th}\phi_{t1} + y_{h1}) + h_{ch}k_{ty2}(-y_{t2} + h_{th}\phi_{t2} + y_{h2})$$
$$- 2k_{tz1}d_{kh}^2(\phi_{t1} + \phi_{t2} - 2\phi_c) = M_{x\_wind} \tag{A10}$$

$$I_{cz}\ddot{\psi}_c - 2k_{ty1}l_c(y_{t1} - y_{t2} - h_{tk}\phi_{t1} + h_{tk}\phi_{t2} - 2l_c\psi_c)$$
$$+ l_c k_{ty2}(-y_{t1} + h_{th}\phi_{t1} + y_{h1}) - l_c k_{ty2}(-y_{t2} + h_{th}\phi_{t2} + y_{h2})$$
$$+ d_{sx}k_{sx}(-2d_{sx}\psi_{t1} + y_{sR1} - y_{sR1}) + d_{sx}k_{sx}(-2d_{sx}\psi_{t2} + y_{sR2} - y_{sL2})$$
$$- 2k_{tx1}d_{kh}^2(\psi_{t1} + \psi_{t2} - 2\psi_c) = I_{cz}v\frac{d}{dt}\left(\frac{1}{R_c}\right) + M_{z\_wind} \tag{A11}$$

$$I_{cy}\ddot{\beta}_c - 2k_{tz1}l_c(z_{t2} - z_{t1} - 2l_c\beta_c) + 2k_{tx1}h_{ck}(2h_{ck}\beta_c + h_{tk}\beta_{t1} + h_{tk}\beta_{t2})$$
$$- h_{cs}k_{sx}(2h_{ts}\beta_{t1} + y_{sL1} + y_{sR1}) - h_{cs}k_{sx}(2h_{ts}\beta_{t2} + y_{sL2} + y_{sR2}) = M_{y\_wind} \tag{A12}$$

The components of aerodynamic loads F_{y_wind}, F_{z_wind}, M_{x_wind}, M_{y_wind}, and M_{z_wind} represent the lateral aerodynamic force, aerodynamic lift, aerodynamic roll moment, aerodynamic pitch moment, and aerodynamic yaw moment, respectively.

(4) For the connecting points of the secondary lateral dampers and yaw dampers,

$$k_{ty2}(y_{ti} - h_{th}\phi_{ti} - y_{hi}) - c_{ty2}[\dot{y}_{hi} - \dot{y}_c - h_{ck}\dot{\phi}_c + (-1)^i l_c\dot{\psi}_c] = 0 \tag{A13}$$

$$k_{sx}[h_{ts}\beta_{ti} + y_{sLi} + d_{sx}(\psi_{ti} + (-1)^i\Phi_{si})] + c_{sx}(h_{cs}\dot{\beta}_c + d_{sx}\dot{\psi}_c + \dot{y}_{sLi}) = 0$$
$$k_{sx}[h_{ts}\beta_{ti} + y_{sRi} - d_{sx}(\psi_{ti} + (-1)^i\Phi_{si})] + c_{sx}(h_{cs}\dot{\beta}_c - d_{sx}\dot{\psi}_c + \dot{y}_{sRi}) = 0 \tag{A14}$$

where $i = 1$ and 2 denote the dampers on the front and the rear frame, respectively.

All physical quantities in Equations (A1) $\sim$ (A14) are defined in Appendix B. The nominal design parameters of vehicle are also provided in Appendix B.

Appendix B. Explanation of parameters and nominal design parameters

Parameters	Explanation and value
Mass of wheelset	$m_w = 1780\,\text{kg}$
Mass of frame	$m_t = 3300\,\text{kg}$
Mass of car body	$m_c = 31{,}374\,\text{kg}$
Roll moment-of-inertia of wheelset	$I_{wx} = 967\,\text{kg·m}^2$
Roll moment-of-inertia of frame	$I_{tx} = 2673\,\text{kg·m}^2$
Roll moment-of-inertia of car body	$I_{cx} = 120{,}800\,\text{kg·m}^2$
Pitch moment-of-inertia of wheelset	$I_{wy} = 118\,\text{kg·m}^2$
Pitch moment-of-inertia of frame	$I_{ty} = 1807\,\text{kg·m}^2$
Pitch moment-of-inertia of car body	$I_{cy} = 1{,}555{,}000\,\text{kg·m}^2$
Yaw moment-of-inertia of wheelset	$I_{wz} = 967\,\text{kg·m}^2$
Yaw moment-of-inertia of frame	$I_{tz} = 3300\,\text{kg·m}^2$
Yaw moment-of-inertia of car body	$I_{cz} = 1{,}467{,}400\,\text{kg·m}^2$
Longitudinal stiffness of primary suspension	$k_{px} = 1.37 \times 10^7\,\text{N/m}$

Parameters	Explanation and value
Lateral stiffness of primary suspension	$k_{py} = 5.49 \times 10^6$ N/m
Vertical stiffness of primary suspension	$k_{pz} = 1.176 \times 10^6$ N/m
Primary vertical damping	$c_{pz} = 19,600$ Ns/m
Half of track gauge	$d_0 = 0.7465$ m
Half of width of primary suspension	$d_{zx} = 1.0$ m
Half of length of primary suspension	$l_t = 0.75$ m
Vertical distance from primary suspension to centre-of-gravity of frame	$h_{tz} = 0.064$ m
Longitudinal stiffness of secondary suspension	$k_{tx1} = 1.597 \times 10^6$ N/m
Lateral stiffness of secondary suspension	$k_{ty1} = 1.597 \times 10^6$ N/m
Vertical stiffness of secondary suspension	$k_{tz1} = 9.9 \times 10^5$ N/m
Half of width of secondary suspension	$d_{kh} = 1.23$ m
Height of secondary suspension above centre-of-gravity of frame	$h_{tk} = 0.39$ m
Vertical distance from secondary suspension to centre-of-gravity of car body	$h_{ck} = 0.62$ m
Half of length of secondary suspension	$l_c = 8.75$ m
Stiffness of spring-damping connecting point of lateral damper	$k_{ty2} = 3.43 \times 10^7$ N/m
Damping of spring-damping connecting point of lateral damper	$c_{ty2} = 1.18 \times 10^5$ Ns/m
Height of lateral damper above centre-of-gravity of frame	$h_{th} = 0.281$ m
Vertical distance from lateral damper to centre-of-gravity of car body	$h_{ch} = 0.719$ m
Stiffness of spring-damping connecting point of yaw damper	$k_{sx} = 8.82 \times 10^6$ N/m
Damping of spring-damping connecting point of yaw damper	$c_{sx} = 2.89 \times 10^5$ Ns/m
Half of width of yaw damper	$d_{sx} = 1.35$ m
Height of yaw damper above centre-of-gravity of frame	$h_{ts} = -0.03$ m
Vertical distance from yaw damper to centre-of-gravity of car body	$h_{cs} = 1.04$ m
Normal wheel radius	$R_0 = 0.43$ m
Axle weight	$W = 1.1 \times 10^5$ N
Left normal contact force of i-th wheelset ($i = 1 \sim 4$)	N_{Li}
Right normal contact force of i-th wheelset ($i = 1 \sim 4$)	N_{Ri}
Left contact angle of i-th wheelset ($i = 1 \sim 4$)	λ_{Li}
Right contact angle of i-th wheelset ($i = 1 \sim 4$)	λ_{Ri}
Left lateral creep forces of i-th wheelset ($i = 1 \sim 4$)	F_{yLi}
Right lateral creep forces of i-th wheelset ($i = 1 \sim 4$)	F_{yRi}
Left longitudinal creep forces of i-th wheelset ($i = 1 \sim 4$)	F_{xLi}
Right longitudinal creep forces of i-th wheelset ($i = 1 \sim 4$)	F_{xRi}
Left creep moment of i-th wheelset ($i = 1 \sim 4$)	M_{zLi}
Right creep moment of i-th wheelset ($i = 1 \sim 4$)	M_{zRi}
normal wheel radius	R_0
Rail radius at the position of i-th wheelset ($i = 1 \sim 4$)	R_{wi}
Rail radius at the position of i-th frame centre ($i = 1, 2$)	R_{ti}
Rail radius at the position of car-body centre	R_c
Superelevation at the position of i-th wheelset ($i = 1 \sim 4$)	ϕ_{rawi}
Superelevation at the position of i-th frame centre ($i = 1, 2$)	ϕ_{rati}
Superelevation at the position of car-body centre	ϕ_{rac}
Relative yaw angle between i-th wheelset and frame due to railway curve ($i = 1 \sim 4$)	Φ_{ai}
Relative yaw angle between i-th frame and car body due to railway curve ($i = 1, 2$)	Φ_{si}